




Cite this: DOI: 10.1039/d5eb00178a

## Resolving the true origin of mossy morphology in aqueous Zn batteries

Jianwen Yu,<sup>a</sup> Zhongxi Zhao,<sup>a</sup> Zhuojun Zhang,<sup>a</sup> Jiangfeng Huang<sup>a</sup> and Peng Tan <sup>\*a,b</sup>

Aqueous zinc-based batteries hold great potential for next-generation energy storage because of their high safety, low cost, and promising electrochemical performance. However, uneven Zn deposition during charging poses a major challenge to their cycling stability. Although dendritic growth has been extensively studied as a typical form of uneven deposition, the evolution and formation mechanism of mossy Zn morphology has remained unclear for a long time. In this work, we move beyond the conventional view that nucleation governs Zn morphology and propose a new mechanism that the interlayer diffusion of adsorbed Zn atoms is the rate-determining step responsible for mossy deposition. This perspective explains why such a morphology tends to form under low polarization and high electrolyte concentrations. Furthermore, although pulse current effectively suppresses dendrites by mitigating ion depletion, the resulting electrolyte enrichment contradicts the suppression of mossy growth. Here, a new explanation for the pulse-induced suppression of mossy zinc morphology is also proposed. Finally, we demonstrate that adding a small amount of potassium stannate ( $K_2SnO_3$ ) to the electrolyte accelerates interlayer diffusion and eliminates mossy deposition even under low polarization and high capacity, offering new insights for optimizing Zn anodes in future battery designs.

Received 19th September 2025,  
Accepted 8th November 2025

DOI: 10.1039/d5eb00178a

rsc.li/EESBatteries

### Broader context

In aqueous Zn batteries, the mossy morphology of zinc deposits leads to severe side reactions and poor reversibility. However, conventional nucleation theory cannot explain the formation of this morphology, and the decoupling of nucleation and growth processes indicates that the growth process determines the emergence of mossy morphology. Here, the zinc growth process is divided into three parts: the reduction of zinc ions, the diffusion of zinc adatoms on the basal plane, and their diffusion to the next basal plane. Experimental and theoretical calculations reveal that interlayer diffusion is the rate-determining step, which is further slowed under low polarization conditions, leading to the accumulation of zinc adatoms on the basal plane. Subsequently, the whiskers formed on the basal plane repeatedly bend and eventually develop into mossy morphology. As one of the suppression strategies, pulse charging provides relaxation time for the interlayer diffusion process, while the potassium stannate additive reduces the thickness of the zinc surface oxide layer and accelerates interlayer diffusion. Both approaches reduce the accumulation of zinc adatoms on the basal plane, resulting in a more uniform and dense layered deposition morphology.

## Introduction

Metallic Zn features abundant reserves, low cost, and a high theoretical specific capacity ( $820 \text{ mAh g}^{-1}$ ), making it a promising anode material.<sup>1–5</sup> In aqueous zinc-based batteries, metallic Zn can be directly used as the anode without the need for binders or conductive agents, offering significant advantages in improving the energy density.<sup>6–8</sup> However, like other metal anode batteries such as lithiummetal systems, zincmetal

batteries face challenges arising from the poor interfacial stability between the metal and the electrolyte. Direct Zn plating in aqueous electrolytes often leads to issues such as interfacial passivation, hydrogen evolution, and uneven deposition.<sup>9–11</sup> Among these, uneven deposition of Zn is one of the most representative failure modes, as it can cause detachment of deposits, uneven stripping, and even penetration of the separator. Previous studies have primarily focused on dendritic morphologies, which are observed in both neutral and alkaline electrolytes and are also common in lithiummetal batteries.<sup>12–14</sup> The conditions that lead to dendrite formation are now well understood: a low electrolyte concentration and high polarization (e.g., high current density or high overpotential) tend to induce dendrites, indicating a diffusion-limited process.<sup>15,16</sup> In contrast, another type of

<sup>a</sup>Department of Thermal Science and Energy Engineering, University of Science and Technology of China (USTC), Hefei 230026, Anhui, China.

E-mail: pengtan@ustc.edu.cn

<sup>b</sup>State Key Laboratory of Fire Science, University of Science and Technology of China (USTC), Hefei 230026, Anhui, China



uneven morphology, mossy deposition, has long been overlooked. Before the application of scanning electron microscopy (SEM) and transmission electron microscopy (TEM), mossy deposition appears as gray-black powder to the eye and is easily confused with other forms. Compared with dendritic deposition, mossy deposition is rarely observed in neutral electrolytes, and some studies have even suggested that mossy deposition does not occur under such conditions.<sup>17,18</sup> This may be attributed to the fact that hydrogen evolution is less favourable in neutral systems than in alkaline systems, which allows the use of a relatively high current density that tends to suppress the formation of mossy deposition.<sup>19</sup> The use of SEM and TEM has revealed clear microstructural differences between dendrites and mossy deposition: dendrites exhibit leaf-like structures, whereas mossy deposition is formed by randomly stacked, curved whiskers approximately 100 nm in diameter.<sup>20</sup> The formation conditions of mossy deposition are nearly the opposite of those of dendrites, as they tend to form under high electrolyte concentrations and low polarization. The mechanisms underlying dendrite formation have been thoroughly studied,<sup>21</sup> many of which are attributed to inhomogeneous nucleation. For example, Lu *et al.* proposed that instantaneous nucleation leads to sparse, coarse nuclei that cause local current density spikes and dendrite formation; they introduced a hydroxyapatite-based interfacial layer that promotes progressive nucleation and generates dense and uniform nuclei to suppress dendrites.<sup>22</sup> Wang *et al.* also demonstrated that the introduction of high-valence cations such as  $\text{Ce}^{3+}$  and  $\text{La}^{3+}$  into the electrolyte can convert instantaneous nucleation into progressive nucleation, thereby mitigating dendrite growth.<sup>23</sup> While Chen *et al.* argued that the nuclei formed *via* instantaneous nucleation grow simultaneously, which is more favourable for subsequent uniform deposition. They employed plasma sputtering and mechanical stretching to treat the Zn anode, thereby inducing instantaneous nucleation and effectively suppressing dendrite growth.<sup>24</sup>

Some researchers have attempted to explain mossy deposition *via* similar nucleation-based frameworks. For example, Li *et al.* observed mossy morphologies under progressive nucleation in  $\text{ZnBr}_2$  electrolytes and suggested that controlling nucleation toward the instantaneous regime is key to forming well-defined bulk Zn and achieving high reversibility.<sup>25</sup> However, these seemingly contradictory results reflect the confusion surrounding the link between the nucleation mode and deposition morphology. It is debatable whether such a fast process, as nucleation typically occurs on the order of seconds, alone can determine the morphology of much longer-term growth.<sup>26</sup> This has prompted us to explore alternative mechanisms beyond nucleation. In addition, some researchers have proposed that an unevenly distributed oxide layer exists on the surface of Zn.<sup>27–29</sup> During deposition, this oxide layer suppresses the layered growth of Zn, and the stripped Zn structures tend to grow out from the pores in the oxide layer. These stripes attract relatively high local current densities, leading to preferential growth and eventual bending, resulting in the for-

mation of mossy Zn deposits. Other studies attributed the formation of mossy morphology to stress-induced mechanisms.<sup>17</sup> During deposition, the reduced Zn atoms diffuse toward surface defects such as grain boundaries, generating compressive stress in the substrate and causing local stress concentration. The growth of mossy Zn is then considered a stress-relief mechanism in which Zn filaments protrude from grain boundaries or other defects to release internal stress. However, while this mechanism is used to explain the formation of mossy deposition, many researchers also believe that stress contributes to dendrite formation.<sup>30,31</sup> This raises an important question: does stress lead to mossy deposition, dendrite growth, or both? Given that the conditions for mossy and dendritic growth are fundamentally different, it is possible that stress relaxation is merely a common result of deposition rather than the root cause of a specific morphology. Furthermore, some researchers have suggested that competing faradaic side reactions during electrodeposition may induce mossy growth.<sup>18</sup> Under low polarization, the rate of side reactions may exceed that of the main Zn deposition reaction, promoting mossy structures. However, this explanation becomes problematic at high concentrations, where side reactions should be suppressed because of the abundance of zincate species; however, mossy deposition becomes even more pronounced. These various hypotheses, while offering valuable insights, still fail to fully explain the formation mechanism of mossy Zn and why it tends to appear under specific conditions.

This work tries to resolve the true origin of mossy morphology in zinc-based batteries. It begins with electrochemical tests and morphological observations, which show that under low polarization and high concentration, the system follows a progressive nucleation mode, whereas under high polarization and low concentration, it follows an instantaneous nucleation mode. By separating the conditions for nucleation and growth, the final deposition morphology is determined to be governed by the growth process rather than the nucleation behavior. The growth of mossy deposition is further investigated *via* SEM, TEM, and X-ray diffraction (XRD). The results reveal that the mossy morphology evolves from initial layered growth dominated by the (002) facet into a polycrystalline structure, and this transition is initiated by whisker-like protrusions emerging from the (002) surface. To elucidate the origin of these protrusions, cyclic voltammetry (CV) measurements and density functional theory (DFT) calculations are performed, which find that interlayer diffusion of reduced Zn adatoms during the deposition steps is the rate-determining step. A slow interlayer diffusion rate leads to the accumulation of Zn atoms on the (002) facet, turning the initial two-dimensional lateral growth into one-dimensional vertical growth, resulting in the formation of protrusions. At high zincate concentrations, more Zn atoms are reduced and thus they accumulate more easily. Under a low overpotential, a thicker surface ZnO layer further slows interlayer diffusion, promoting protrusion formation. To address the formation of mossy morphology, two mitigation strategies are proposed: one is the application



of pulse deposition, a method widely used to suppress dendrite formation, but the mechanism is totally different; the other approach involves introducing a small amount of  $K_2SnO_3$  into the electrolyte to enable co-deposition of Zn and Sn, from which the high redox potential of Sn suppresses the formation of surface  $ZnO$ , thereby enhancing interlayer diffusion and producing a denser and more uniform morphology. This work reveals the formation mechanism of mossy deposition morphology in aqueous zinc-based batteries, providing insights for the development of strategies to optimize the performance of Zn anodes.

## Results and discussion

### The influence of current density and concentration on morphology and nucleation

To identify the conditions that trigger mossy morphology, Zn depositions were formed at various zincate ion concentrations and current densities while maintaining a constant deposition capacity. The deposited morphology exhibits a strong dependence on both electrolyte concentration and

current density, as shown in Fig. 1a–g. With increasing concentrations from 0.1 M to 0.4 M (Fig. 1a–d), the structure transitions from dendritic to smooth layered stacking, then to filamentous Zn, and finally to fully developed mossy deposition. Similarly, as the current density decreases from  $30 \text{ mA cm}^{-2}$  to  $10 \text{ mA cm}^{-2}$  (Fig. 1d–g), the morphology evolves from dendrites through layered stacking to complete mossy coverage, confirming that mossy morphology preferentially forms under high-concentration and low-polarization conditions. To investigate whether the mossy deposition is related to the nucleation process, CV tests were conducted at different concentrations (Fig. 1h). The nucleation overpotential is defined as the voltage difference between the intersection of the forward and reverse scans and the initial drop point in the reverse scan.<sup>32–34</sup> As shown in the inset, the nucleation overpotentials for 0.1, 0.2, 0.3, and 0.4 M are 75.5, 65.4, 52.2, and 50.8 mV, respectively, indicating a decrease in the nucleation overpotential with increasing concentration. The effect of polarization on the nucleation overpotential was evaluated *via* galvanostatic tests,<sup>35–37</sup> as shown in Fig. 1i. The nucleation overpotentials at 1, 5, and  $10 \text{ mA cm}^{-2}$  are 12.2, 13.6, and 22.2 mV, respectively, suggesting

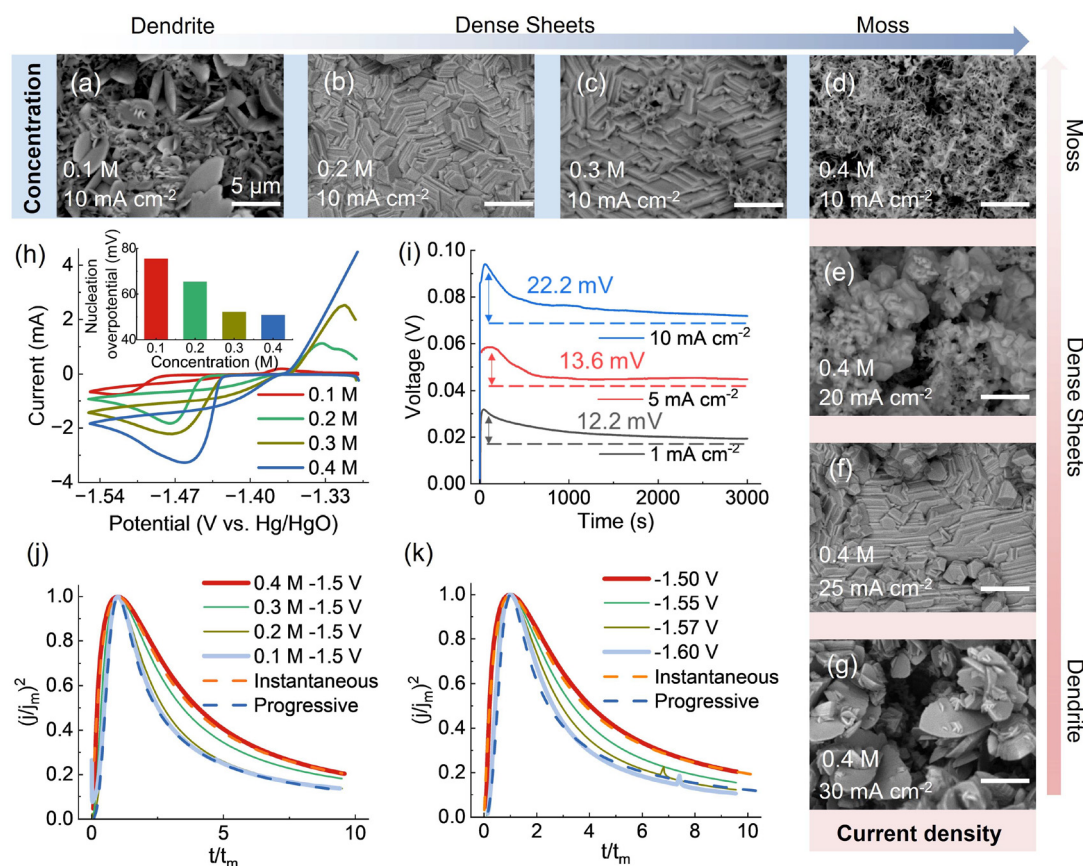


**Fig. 1** Influence of different current densities and concentrations on morphology and nucleation. (a–d) Morphologies at concentrations of (a) 0.1, (b) 0.2, (c) 0.3 and (d) 0.4 M. (e–g) Morphologies at current densities of (e)  $20 \text{ mA cm}^{-2}$ , (f)  $25 \text{ mA cm}^{-2}$  and (g)  $30 \text{ mA cm}^{-2}$ . (h and i) Nucleation overpotentials at different (h) concentrations and (i) current densities. (j and k) Nucleation modes at different (j) concentrations and (k) current densities.



that lower polarization leads to a lower nucleation overpotential. The specific nucleation modes under different conditions were determined *via* chronoamperometry (Fig. S1 and S2).<sup>38–40</sup> The current peaks appear within a few seconds after voltage application, indicating that nucleation occurs on a very short timescale. After normalization, the experimental curves were compared with theoretical models of nucleation. As shown in Fig. 1j, the behavior at 0.1 M matches that of progressive nucleation, whereas 0.2 and 0.3 M exhibit characteristics between progressive and instantaneous nucleation, and 0.4 M fits the instantaneous nucleation model. This suggests that higher concentrations favour instantaneous nucleation, whereas lower concentrations tend toward progressive nucleation. The effect of polarization on the nucleation mode is shown in Fig. 1k. At  $-1.50$  V, the nucleation follows the instantaneous model, whereas at  $-1.60$  V, it follows the progressive model, indicating that low polarization favours instantaneous nucleation, whereas high polarization favours progressive nucleation.

### The nucleation mechanisms at different current densities and concentrations

To enhance the reliability of the conclusions, in addition to electrochemical testing, morphological observations were also employed to elucidate the nucleation modes under different conditions. In general, instantaneous nucleation occurs extremely rapidly within a very short time. After nucleation is complete, the nuclei grow in size, and the number of nuclei in the later stage changes little compared with that in the earlier stage; only their size increases. In contrast, progressive nucleation involves the continuous formation of new nuclei throughout the nucleation process, resulting in a significant increase in the number of nuclei over time.<sup>41,42</sup> We conducted SEM imaging of the electrodes at different stages of nucleation. The glassy carbon electrode was cleaned with hydrochloric acid and deionized water before each experiment, then dried and polished with suede, and finally wiped clean with lint-free paper. To guarantee the same deposition capacity for each comparison group, galvanostatic deposition was utilized rather than potentiostatic deposition. At 0.4 M with a low current density of  $10 \text{ mA cm}^{-2}$ , the nucleus count remained nearly constant, decreasing only slightly from 799 to 679 between 1 s and 2 s (Fig. 2a, b and g), indicative of instantaneous nucleation. The slight decrease may be attributed to coalescence during the growth of the nuclei. In contrast, under high polarization at the same concentration ( $20 \text{ mA cm}^{-2}$ ), the number of nuclei surged from 2084 to 4959 in just 0.5 s (Fig. 2c, d and g), demonstrating clear progressive nucleation behavior. Similarly, at a low concentration of 0.1 M with  $10 \text{ mA cm}^{-2}$ , the nucleus count also showed a significant increase from 245 to 1061 over 1 s (Fig. 2e–g), confirming a progressive nucleation mode under these conditions. These morphological observations are in full agreement with the electrochemical measurements. In previous electrochemical analyses,<sup>43</sup> the nucleation overpotential was found to be

related to the critical nucleus size according to the following relationship:

$$r = 2 \frac{\gamma V_m}{F|\eta|}$$

where  $r$ ,  $\gamma$ ,  $V_m$ ,  $F$ , and  $\eta$  represent the critical radius, the interfacial surface energy between Zn and the electrolyte, the molar mass of Zn, the Faraday constant, and the nucleation overpotential, respectively, indicating that the critical radius is inversely proportional to the nucleation overpotential. As shown in Fig. 2h, the average nucleus size in the second stage under three different conditions was also statistically analysed. For 0.4 M with  $10 \text{ mA cm}^{-2}$ , 0.4 M with  $20 \text{ mA cm}^{-2}$  and 0.1 M with  $10 \text{ mA cm}^{-2}$ , the average nucleus radii were  $0.191 \text{ }\mu\text{m}$ ,  $0.170 \text{ }\mu\text{m}$ , and  $0.184 \text{ }\mu\text{m}$ , respectively. This indicates that the greater the polarization, the smaller the nuclei; the lower the concentration, the smaller the nuclei. These results align with previous findings that higher polarizations and lower concentrations correspond to higher nucleation overpotentials. Fig. 2i shows the influence of polarization on the nucleation mode. Compared with low polarization, higher polarization activates more nucleation sites. However, since the total number of Zn atoms available for deposition remains the same at the same concentration, under low polarization, each nucleation site receives a more uniform and larger allocation of Zn atoms, whereas under high polarization, the distribution becomes uneven, and each site receives fewer atoms. This leads to faster nucleation and larger nuclei under low polarization, corresponding to instantaneous nucleation, whereas high polarization leads to progressive nucleation. When the polarization remains constant and the number of nucleation sites does not change, low-concentration conditions cause Zn atom allocation per nucleation site to be uneven and less than under high-concentration conditions (Fig. 2j). As previously explained, this results in instantaneous nucleation with larger nuclei at high concentrations and progressive nucleation with smaller nuclei at low concentrations. To summarize, the effects of concentration and polarization on nucleation have been clarified. Interestingly, high concentration and low polarization lead to mossy morphology, and both conditions correspond to instantaneous nucleation with larger nuclei. This raises the question: is instantaneous nucleation responsible for the formation of mossy morphology?

### The influence of the nucleation and growth processes on the mossy structure

To investigate whether nucleation affects the morphology, four sets of experiments were designed with the same total deposited capacity. First, deposition performed solely at  $10 \text{ mA cm}^{-2}$  for 600 s resulted in a mossy morphology (Fig. 3a). When the same capacity was deposited at a higher current density of  $25 \text{ mA cm}^{-2}$  for 240 s, the morphology changed to a gravel-like structure (Fig. 3b). Next, the deposition process was separated into the nucleation and growth stages. As illustrated in Fig. 3c,





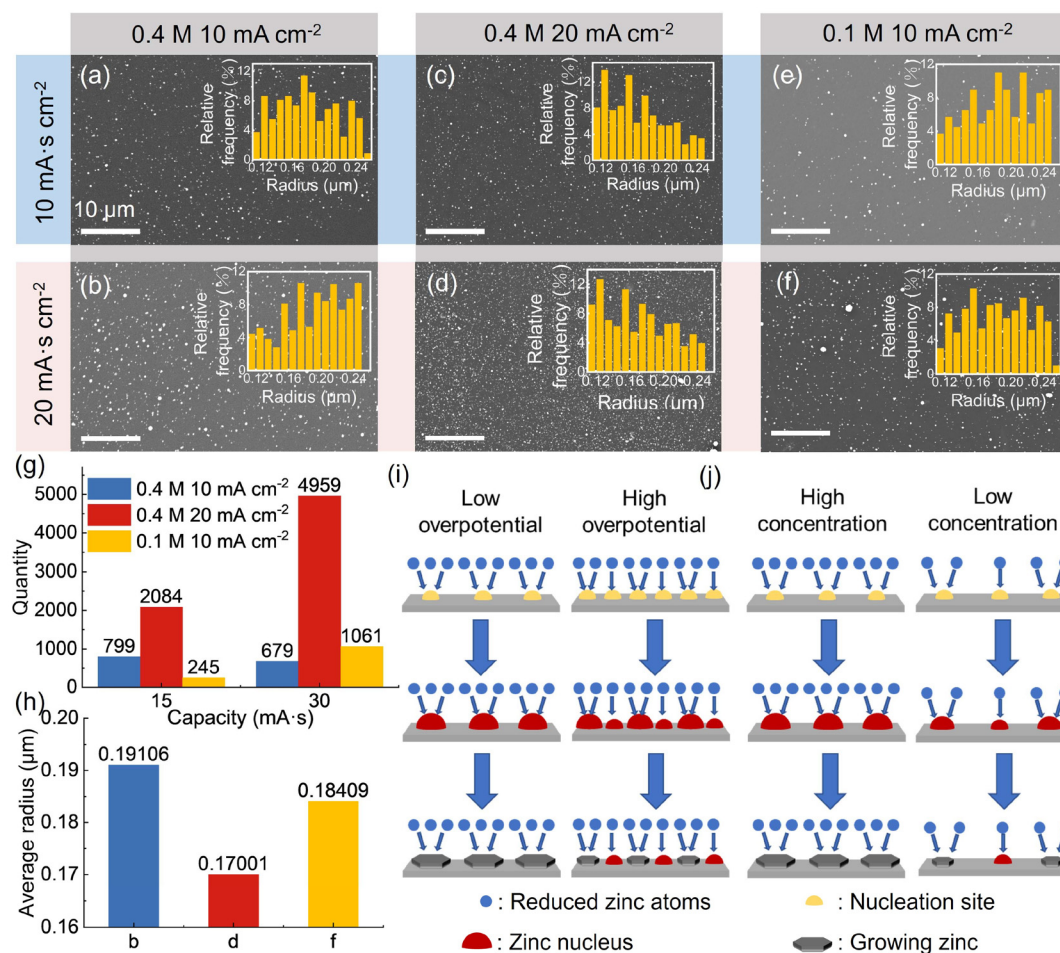


**Fig. 2** Morphological observations of nucleation under different conditions. (a and b) Morphologies at 0.4 M under 10 mA cm<sup>-2</sup> for (a) 1 s and (b) 2 s. (c and d) Morphologies at 0.4 M under 20 mA cm<sup>-2</sup> for (c) 0.5 s and (d) 1 s. (e and f) Morphologies at 0.1 M under 10 mA cm<sup>-2</sup> for (e) 1 s and (f) 2 s. (g) Nucleus number statistics. (h) Average nucleus radius statistics in (b), (d), and (f). (i and j) Schematic diagram of nucleation modes under (i) different polarizations and (j) concentrations.

nucleation at 10 mA cm<sup>-2</sup> for 50 s followed by growth at 25 mA cm<sup>-2</sup> for 220 s produced a gravel-like structure at Point B. When this sequence was reversed, with nucleation at 25 mA cm<sup>-2</sup> for 20 s followed by growth at 10 mA cm<sup>-2</sup> for 550 s, the resulting deposition was mossy, as shown in Fig. 3d. Subsequently, another experiment was conducted to examine the reversibility of the mossy morphology. Deposition was first carried out at 10 mA cm<sup>-2</sup> for 600 s, then at 25 mA cm<sup>-2</sup> for 240 s. The deposit remained mossy (Fig. 3e). Finally, the influence of the substrate was investigated by depositing first at 25 mA cm<sup>-2</sup> for 240 s, followed by 10 mA cm<sup>-2</sup> for 600 s, which also resulted in a mossy morphology (Fig. 3f). Fig. 3g summarizes these experiments: nucleation at high polarization followed by growth at low polarization results in a mossy morphology, whereas nucleation at low polarization followed by growth at high polarization produces a gravel-like morphology. This finding indicates that the formation of a mossy morphology is unrelated to the nucleation stage but depends on the growth stage. Once a mossy morphology forms, applying

high polarization afterward does not reverse it back to a gravel-like morphology. Furthermore, even if the initial deposit on the substrate is gravel-like, a mossy morphology will appear once the conditions favour its formation, indicating that the appearance of mossy morphology is independent of the substrate.

### The growth process of the mossy morphology

The growth of mossy Zn was further investigated. The morphological evolution during deposition at 20 mA cm<sup>-2</sup> reveals a distinct progression from small particles to mossy coverage over time. Fig. 4a and b document the transition after 20 and 80 s of deposition, respectively, showing initial small particles developing into layered stacked blocks. During the intermediate stage (80 s), abundant hexagonal basal facets identified as the (002) planes are clearly exposed (Fig. S3), before the surface ultimately becomes covered with mossy deposition after 400 s, as shown in Fig. 4c. Fig. 4d shows the XRD patterns at these three time points, and the peak intensity ratio analysis



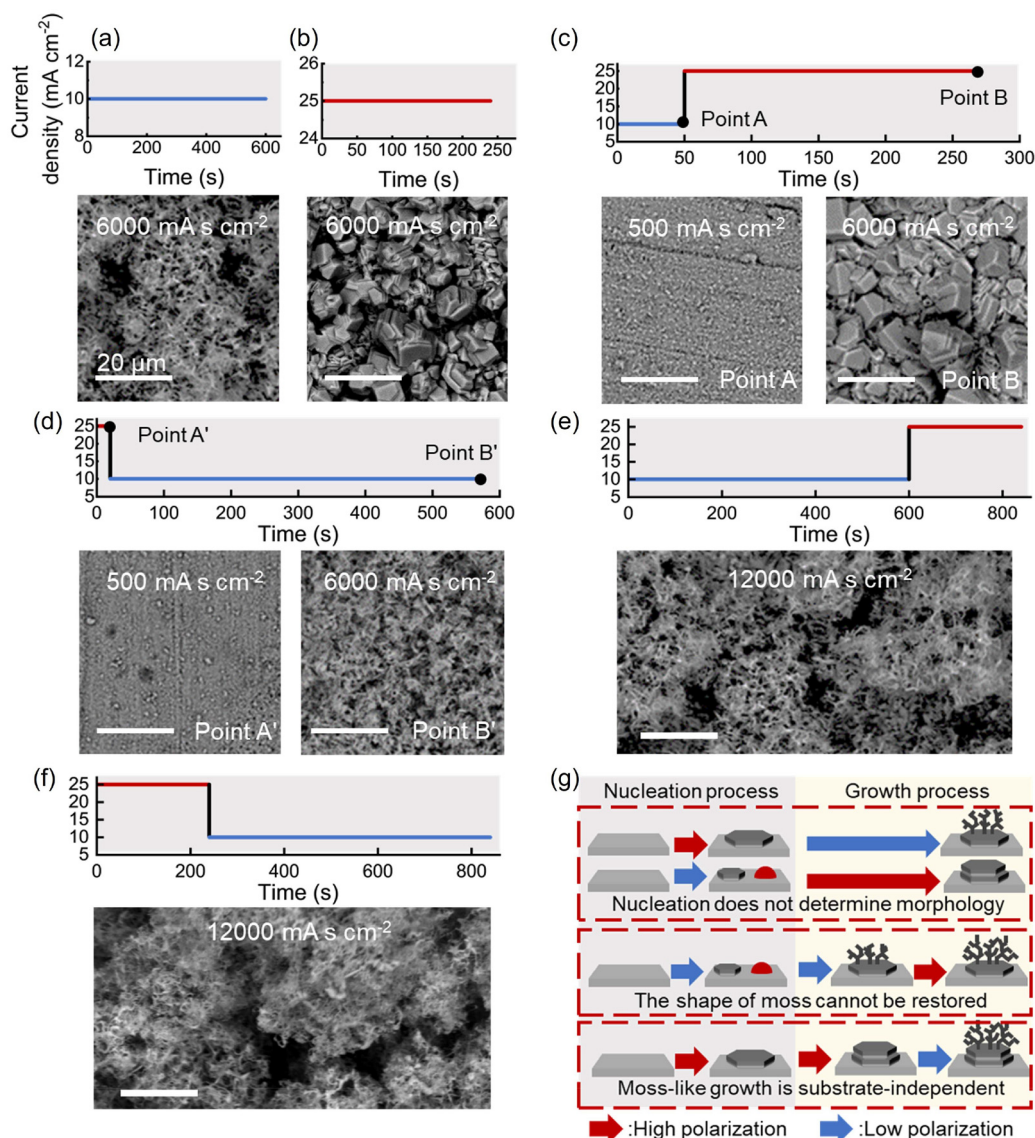


**Fig. 3** Influence of nucleation and growth on morphology, the reversibility of mossy deposition, and the effect of the substrate on mossy formation. (a and b) Morphologies after charging at (a)  $10 \text{ mA cm}^{-2}$  for 10 min and at (b)  $25 \text{ mA cm}^{-2}$  for 4 min. (c) Charged at  $10 \text{ mA cm}^{-2}$  for 50 s followed by  $25 \text{ mA cm}^{-2}$  for 220 s. (d) Charged at  $25 \text{ mA cm}^{-2}$  for 20 s followed by  $10 \text{ mA cm}^{-2}$  for 550 s. (e) Charged at  $10 \text{ mA cm}^{-2}$  for 10 min followed by  $25 \text{ mA cm}^{-2}$  for 4 min. (f) Charged at  $25 \text{ mA cm}^{-2}$  for 4 min followed by  $10 \text{ mA cm}^{-2}$  for 10 min. (g) Schematic summary.

is given in Fig. 4e. After the initial 20 s, the intensity ratios of the (002) peak to the (100) and (101) peaks are 4.11 and 11.62, respectively. After 80 s, the ratios significantly increase to 30.17 and 22.81, indicating that the (002) facet had become the dominant crystal facet during this stage. This is attributed to the close-packed (002) facet having low surface energy and favourable chemical properties.<sup>44,45</sup> When Zn adatoms adsorb onto the (002) Zn surface, they have a relatively low probability of aggregating to form a new layer due to the large nucleation energy barrier involved, which corresponds well with the abundant hexagonal facets observed in Fig. 4b. However, after 400 s, the (002) peak intensity ratios relative to the (100) and (101) peaks decrease to 1.71 and 0.51, respectively, indicating the disappearance of (002) dominance and the formation of dis-

ordered polycrystalline mossy deposition. To explain how this polycrystalline or mossy structure forms, TEM imaging was performed on freshly grown whiskers and their transition into a mossy morphology. As shown in Fig. 4f, step-like morphologies appear on the deposited Zn particles, with a whisker protruding from the top step layer that is approximately 100 nm in diameter, which is consistent with previous reports.<sup>20</sup> Owing to the sample thickness, high-resolution TEM (HR-TEM) imaging was not feasible; however, the SEM image in Fig. S4 shows that these initial mossy formations originate on the hexagonal facets, and previous studies have reported that whisker nucleation starts on the (002) facet.<sup>19,46</sup> In Fig. 4g, the formed whiskers subsequently begin to bend, and after a series of bends, their morphology appears mossy at the micron



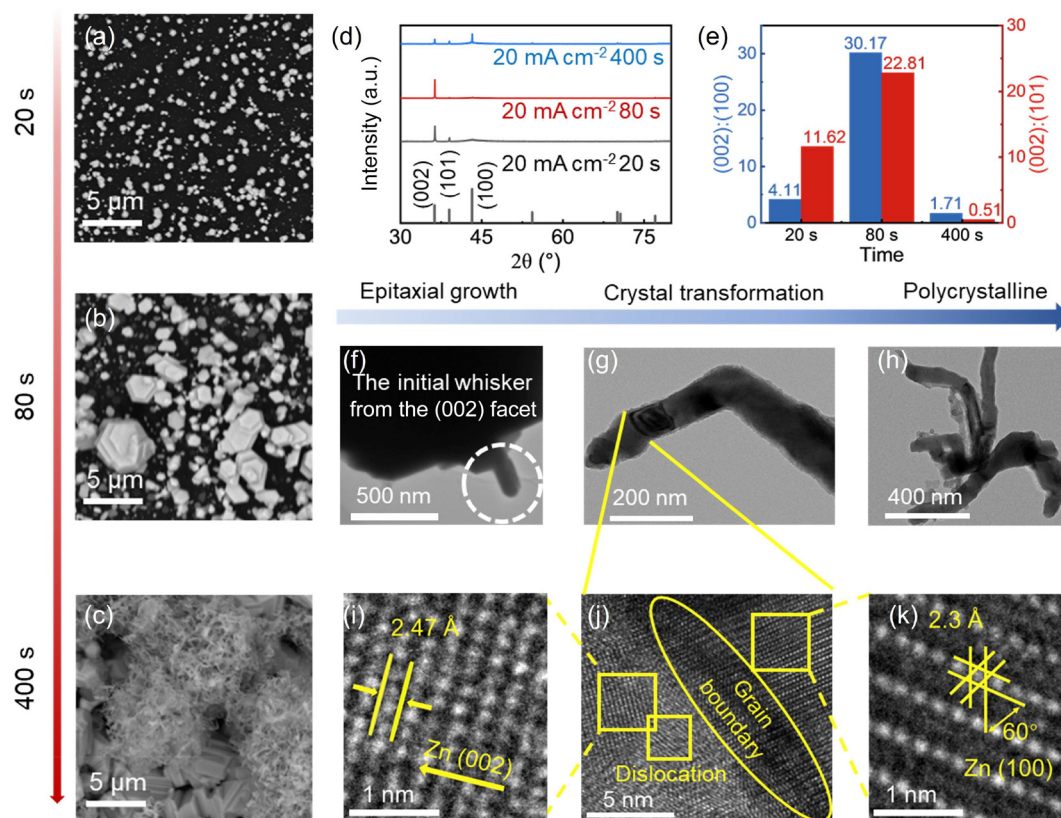


**Fig. 4** Mossy deposition growth process. (a–c) SEM morphologies after deposition at  $20 \text{ mA cm}^{-2}$  for (a) 20, (b) 80, and (c) 400 s. (d) XRD patterns at three different stages. (e) Comparative analysis of peak intensities at the three stages. (f–h) TEM images of the (f) whisker initiation, (g) growth, and (h) completion stages. (i–k) HR-TEM images at the (i) left, (j) center and (k) right sides of the black boundary line in (g).

scale, as shown in Fig. 4h. To clarify the crystal facet transformation during this process, HR-TEM was performed in the bending region, as shown in Fig. 4g. Analysis of the lattice spacing to the left of the bending region yields  $2.47 \text{ \AA}$  (Fig. 4i and Fig. S5), corresponding to the Zn (002) orientation, and a clear grain boundary is observed at the bend (Fig. 4j); however, on the right, the lattice spacing is  $2.3 \text{ \AA}$  (Fig. 4k and Fig. S6), corresponding to the Zn (100) orientation. Additionally, Fig. 4g reveals distinct dark lines within the whiskers, caused by screw dislocations twisting the lattice and resulting in additional electron absorption.<sup>17</sup> This is also evident in Fig. 4j, where the crystallographic orientation within the square below the (002) region differs markedly from the (002) orientation itself. This indicates that lattice dislocations occur during the elongation of whisker-like deposits. Owing to the small radius of the whiskers, these unavoidable dislocations readily induce crystal orientation changes and bending, ultimately leading to the formation of a polycrystalline mossy morphology.

#### Mechanistic analysis of initial whisker formation and the effect of concentration

After the growth process of the mossy morphology was clarified, attention was given to the origin of the initial whiskers observed on the (002) facet. To investigate this, CV tests at

different scan rates were conducted in 0.1 M and 0.4 M electrolytes, as shown in Fig. 5a. The data were processed by plotting the peak current against the square root of the scan rate. For both electrolytes, the fitted curves follow a quadratic function (Fig. 5b), indicating that the Zn deposition process in both cases is diffusion controlled with a fast charge transfer step.<sup>25</sup> This means that the zincate ions are rapidly reduced to Zn atoms. As previously mentioned, the initial whiskers grow from terrace structures on the (002) facet. To further understand this, a stepped-surface model was constructed for the DFT calculations (Fig. 5c). The core of the model consists of a  $6 \times 6 \times 4$  Zn atom slab. On the top and right surfaces of this Zn slab, a layer composed of  $3 \times 11$  Zn and oxygen atoms was added to achieve the Zn step covered by a ZnO film. This configuration explains the inevitable corrosion and passivation of Zn by the alkaline electrolyte under basic conditions ( $\text{Zn} + 2\text{OH}^- \rightarrow \text{ZnO} + \text{H}_2\text{O} + 2\text{e}^-$  and  $\text{Zn}(\text{OH})_4^{2-} \rightarrow \text{ZnO} + \text{H}_2\text{O} + 2\text{OH}^-$ ). Numerous studies, along with subsequent characterization, have confirmed the presence of ZnO on the surface of Zn.<sup>21,47</sup> In the constructed model, the upper surface of the step corresponds to the (002) facet, whereas the side corresponds to the (100) facet. The diffusion energy barriers of reduced Zn adatoms, which are adsorbed but not yet incorporated into the lattice, were then calculated for diffusion across





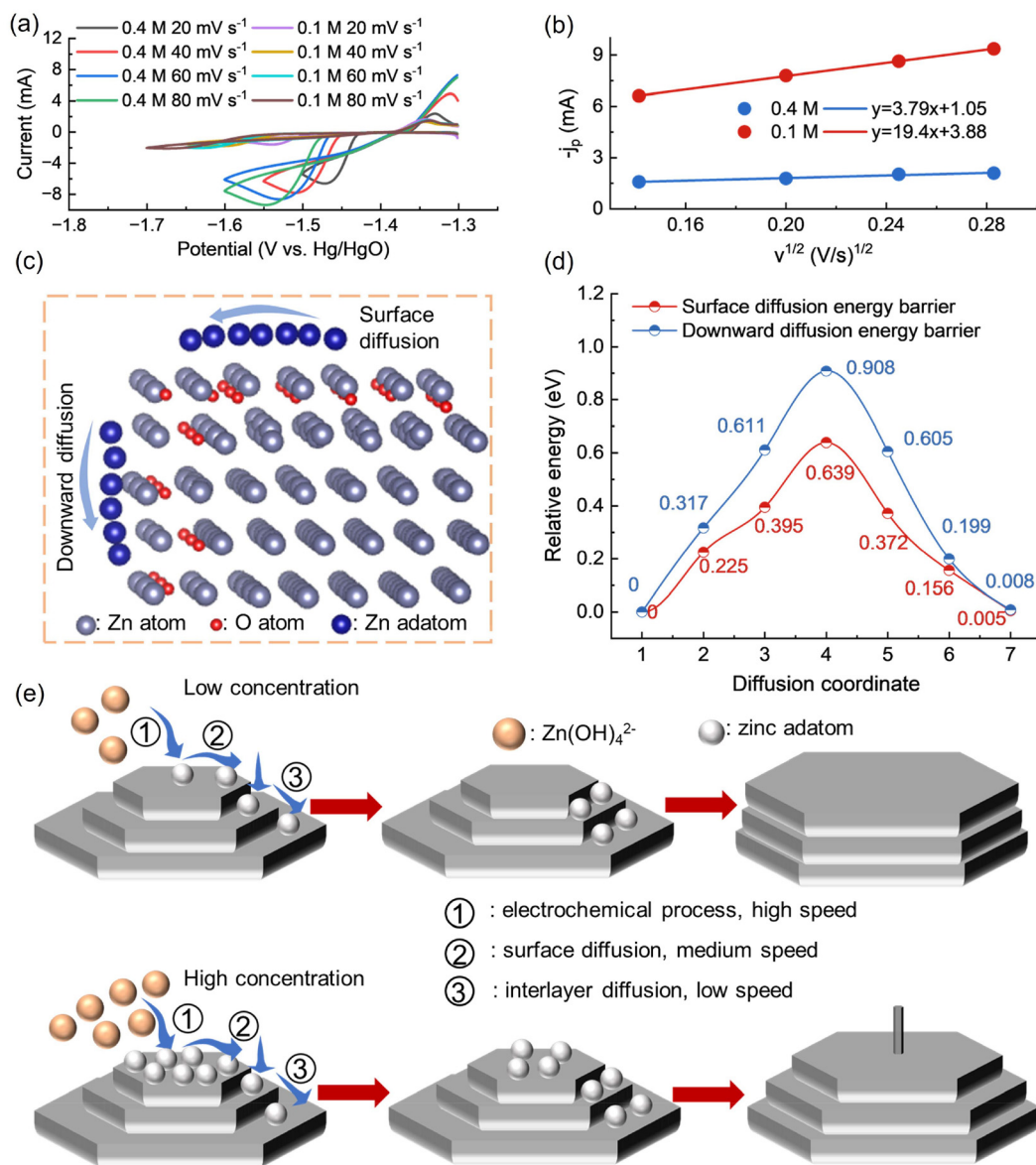


**Fig. 5** Mechanistic analysis of initial whisker formation and the influence of concentration and polarization levels. (a) CV at different concentrations and scan rates. (b) Relationship between peak currents and the square root of scan rates. (c) Surface and interlayer diffusion model with a layer of zinc oxide. (d) Surface and interlayer diffusion energy barriers with a layer of zinc oxide. (e) Schematic diagram of the effect of concentration on the mossy deposition formation.

the (002) facet and downwards along the (100) facet toward the lower step. The diffusion paths are shown by the blue spheres. The decision to calculate the diffusion and interlayer energy barriers on the (002) plane was based on our XRD data, which indicated its dominant presence. This approach is also supported by the work of Mitsuhashi *et al.*, who demonstrated through electrodeposition experiments on (002) single-crystal zinc that mossy structures originate from the (002) plane, as illustrated in Fig. S7. The calculated diffusion energy barriers reveal a significantly higher energy barrier for interlayer diffusion along the (100) facet (0.908 eV) compared to lateral diffusion on the (002) basal plane (0.639 eV) (Fig. 5d). This finding indicates that vertical diffusion to the lower step is

slower than lateral diffusion on the basal facet. Based on the above experiments and calculations, we can interpret the mechanism of mossy morphology formation and explain why it occurs more readily at high concentrations. As shown in Fig. 5e, the Zn electrodeposition process can be divided into three steps: the first step is the charge transfer reaction, in which zincate ions are reduced to Zn atoms that adsorb onto the substrate surface, and this step is the fastest. The second step involves the surface diffusion of Zn adatoms across the basal facet, which is relatively slow. The third step is the downward diffusion of Zn adatoms to the lower layer, which is the slowest and thus the rate-determining step. At low concentrations, fewer Zn adatoms are generated in the first step, and





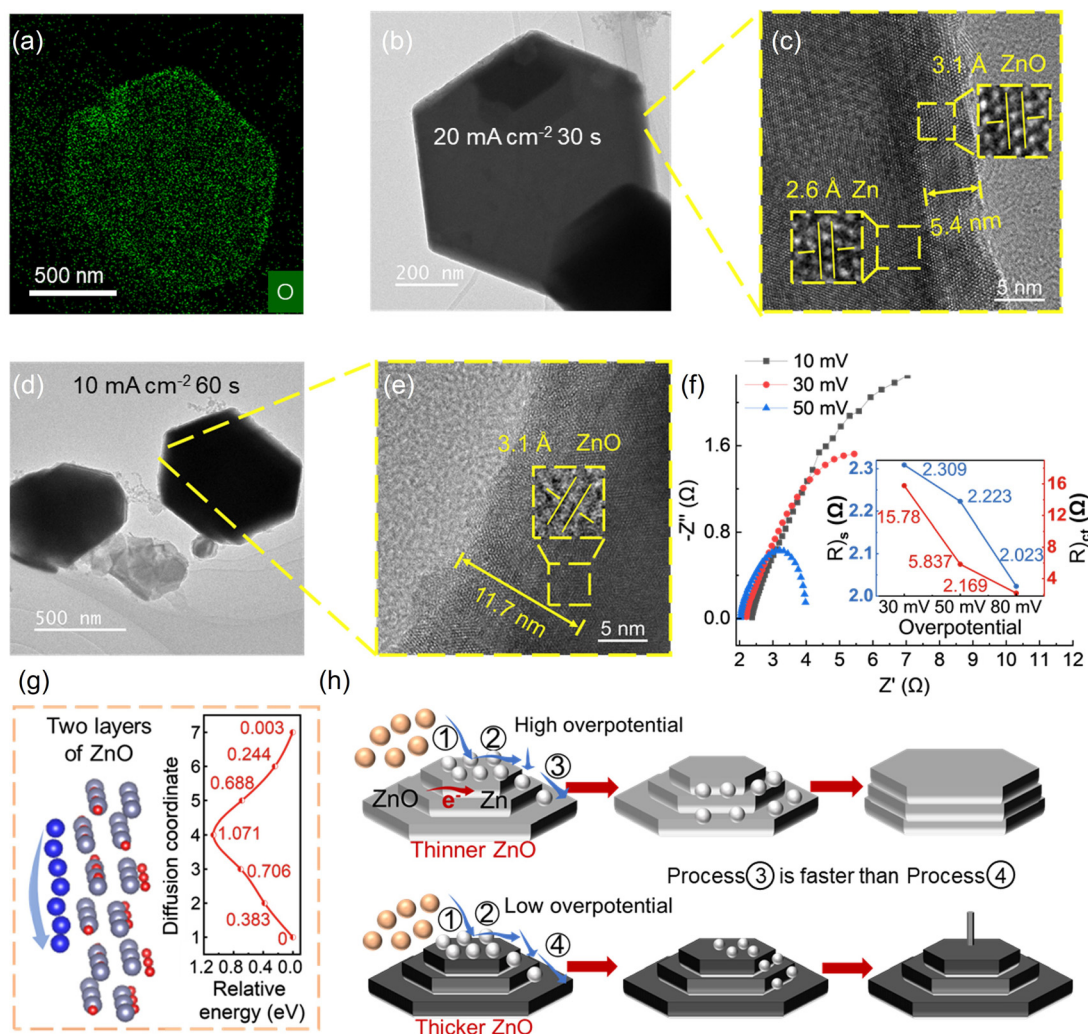


**Fig. 6** (a) Oxygen element mapping. (b) TEM image at  $20 \text{ mA cm}^{-2}$  for 30 s. (c) HR-TEM image of (b). (d) TEM image at  $10 \text{ mA cm}^{-2}$  for 60 s. (e) HR-TEM image of (d). (f) EIS at different bias voltages. (g) Interlayer diffusion with two layers of zinc oxide. (h) Schematic diagram of the effect of polarization.

the diffusion rates in the second and third steps are sufficient to allow them to migrate to the lower layers. This leads to lateral two-dimensional growth on the surface, forming a gravel-like morphology macroscopically. However, at high concentrations, many Zn adatoms are produced in the first step. Since the third step is too slow to accommodate them, Zn adatoms accumulate on the basal facet. This accumulation lowers the nucleation barrier on the surface and promotes growth directly on the top surface, which becomes increasingly confined, ultimately leading to vertical one-dimensional growth in the form of whiskers.

### The effect of polarization

The influence of polarization on mossy morphology is primarily explained by differences in the thickness of the oxide layer. Energy-dispersive X-ray spectroscopy (EDS) mapping of the deposited Zn (Fig. 6a) clearly shows the presence of oxygen. TEM imaging was conducted after deposition under high-polariz-

ation conditions (current density of  $20 \text{ mA cm}^{-2}$  and deposition time of 30 s), as shown in Fig. 6b. The HR-TEM image of the edge of a hexagonal structure (Fig. 6c) reveals a distinct dark boundary. Lattice spacing analysis on either side of the boundary shows  $2.6 \text{ \AA}$  on the interior (Fig. S8, corresponding to metallic Zn) and  $3.1 \text{ \AA}$  on the exterior (Fig. S9, corresponding to ZnO). The thickness of the ZnO layer at the outer edge was found to be approximately  $5.4 \text{ nm}$ . Subsequently, deposition was performed at a lower polarization (Fig. 6d,  $10 \text{ mA cm}^{-2}$  for 60 s). The HR-TEM image of the hexagonal edge under these conditions shows no clear boundaries (Fig. 6e). Lattice spacing analysis at  $11.7 \text{ nm}$  from the edge reveals a spacing of  $3.1 \text{ \AA}$ , as shown in Fig. S10, indicating the presence of ZnO and suggesting that the Zn deposited under low polarization is covered by a thicker ZnO layer. In addition, EIS tests were carried out under different applied potentials, and the corresponding equivalent circuit model used for fitting is shown in Fig. S11. As shown by the Nyquist plots in



Fig. 6f, increasing the applied bias voltage leads to a decrease in the intercept on the X-axis. The inset highlights that at bias voltages of 10, 30, and 50 mV, the corresponding ohmic resistances are 2.309, 2.223, and 2.203  $\Omega$ , respectively. Moreover, the diameters of the semicircles, which represent the charge transfer resistance, also decrease with increasing bias, measuring 15.78, 5.84, and 2.17  $\Omega$ , respectively. This trend indicates that at higher bias voltages, the oxide layer is reduced, resulting in increased conductivity. A thinner oxide layer also facilitates charge transfer, further confirming that the degree of polarization influences the thickness of the oxide layer. On this basis, the ZnO thickness in the DFT model was increased to two layers, and the energy barrier for downward diffusion through the (100) facet was recalculated, as shown in Fig. 6g. The maximum diffusion energy barrier increases to 1.071 eV, compared to 0.908 eV for the monolayer ZnO case. This indicates that a thicker oxide layer hinders interlayer diffusion. As illustrated in Fig. 6h, under high polarization, the oxide layer is reduced, promoting faster interlayer diffusion and enabling the formation of gravel-like deposits. In contrast, under low polarization, a thicker ZnO layer leads to Zn atom accumulation on the basal facet, initiating whisker growth. As previously discussed, the mossy morphology is rarely observed under neutral conditions. To explain this phenomenon, Tafel tests were conducted in five electrolytes: 6 M ZnO + 0.4 M KOH, 2.8 M KCl + 0.4 M ZnCl<sub>2</sub>, 2 M ZnSO<sub>4</sub>, 1 M ZnSO<sub>4</sub> and 2 M Zn(OTf)<sub>2</sub> (Fig. S12), and their Tafel slopes were fitted to be 7.8, 13.8, 23.2, 25.3 and 34.34, respectively; a larger Tafel slope corresponds to slower electrochemical kinetics, indicating a progressive decrease in the reaction kinetics. The deposition morphologies observed in these electrolytes are shown in Fig. S13a–e and include mossy, mossy, partially mossy, gravel-like structures, and radiating block-like morphologies, respectively. We attribute this to the significantly slower reaction kinetics in neutral electrolytes, especially in lower-concentration ZnSO<sub>4</sub> solutions and Zn(OTf)<sub>2</sub> solution. The sluggish charge transfer step limits the formation and accumulation of Zn adatoms on the basal facet, making mossy morphology less likely to form than in alkaline conditions.

### Pulse charging and addition of the K<sub>2</sub>SnO<sub>3</sub> additive

From the formation mechanism of the mossy deposition, it is now possible to regulate it from a mechanistic perspective. To provide sufficient time for interlayer diffusion, pulsed charging was applied during the deposition process, as shown in Fig. 7a. The experimental group was charged with a frequency of 5 Hz and a duty cycle of 50%, *i.e.*, 100 ms charging followed by 100 ms resting. To ensure the same total charge capacity, the non-pulsed group was charged for 10 min, whereas the pulsed group was charged for 20 min. As shown in the voltage profiles in Fig. 7b, the non-pulsed group exhibits a higher voltage, indicating that pulsed charging can also increase the concentration of zincate ions near the electrode. Morphological observations reveal mossy deposition under continuous charging (Fig. 7c), while pulsed charging at 5 Hz results in a gravel-like morphology (Fig. 7d). Varying the pulse frequency shows that both high (50

Hz) and low (0.5 Hz) frequencies lead to the reappearance of mossy deposition, as shown in Fig. 7e and f, suggesting a frequency-dependent effect. Pulse charging, as a charging strategy, has proved highly effective in suppressing dendrite formation. This is because the relaxation periods during pulsing allow higher ion concentrations to replenish the electrode surface *via* diffusion, effectively mitigating ion depletion that leads to dendritic growth. However, for mossy morphology, elevated ion concentrations conversely promote its formation. Therefore, the conventional theory used to explain dendrite suppression is not applicable in this context. Herein, this work proposes a new mechanistic explanation. A schematic summary is presented in Fig. 7g and Fig. S14: at an appropriate frequency, the pulsed charging introduces relaxation intervals during which the charge transfer process ceases, allowing sufficient time for the adsorbed Zn atoms to diffuse downwards. This effectively prevents excessive accumulation of surface atoms and promotes lateral surface growth instead of two-dimensional columnar growth, thereby suppressing the initial whisker formation that leads to mossy morphology. However, at low frequencies, the prolonged relaxation allows more zincate ions to diffuse from the bulk solution to the electrode surface, which are then rapidly reduced during the next pulse, resulting in Zn atom accumulation and one-dimensional vertical growth. At high frequencies, the short relaxation time is insufficient to support interlayer diffusion, which also leads to mossy deposition. To validate the universality of the pulse strategy, relevant verification experiments were also conducted in ZnCl<sub>2</sub> electrolyte and commonly used button batteries, as shown in Fig. S15 and S16. In addition, the use of K<sub>2</sub>SnO<sub>3</sub> as an additive has also proved to be effective. As shown in Fig. 7h, cyclic voltammetry reveals that the reduction peak of Zn shifts from −1.460 V to −1.447 V upon addition of K<sub>2</sub>SnO<sub>3</sub>, whereas the peak current increases from 3.35 mA to 4.06 mA, suggesting enhanced Zn reduction. Another peak appearing at −1.420 V is attributed to the co-deposition of Sn. Elemental mapping confirms the presence of Sn in the deposits (Fig. 7i). The HR-TEM image of the deposit edge (Fig. 7j) under conditions of 10 mA cm<sup>−2</sup> for 60 s reveals that the oxide layer thickness decreases significantly after K<sub>2</sub>SnO<sub>3</sub> addition, from more than 11.7 nm to 2.5 nm. This is because Sn is more inert than Zn and suppresses surface oxidation. When deposition was performed with this electrolyte, mossy deposition that previously formed after 10 minutes of deposition at 10 mA cm<sup>−2</sup> no longer appears even after 1 hour (Fig. 7k). Furthermore, at very low polarization (2 mA cm<sup>−2</sup> for 1 h, Fig. 7l), no mossy structures are observed, indicating that Sn addition reduces the oxide layer thickness and accelerates interlayer diffusion, thereby suppressing mossy growth. The corrosion resistance of the deposited materials obtained from the two electrolytes was further compared. After deposition at 10 mA cm<sup>−2</sup> for 10 minutes, corrosion Tafel tests were conducted (Fig. 7m). With the addition of K<sub>2</sub>SnO<sub>3</sub>, the corrosion potential shifts positively from −19.8 mV to −15.0 mV, and the corrosion current also decreases, indicating improved corrosion resistance of the deposits after K<sub>2</sub>SnO<sub>3</sub> was introduced. When subjected to prolonged charging at 10 mA cm<sup>−2</sup> in both electrolytes, the voltage of the original elec-



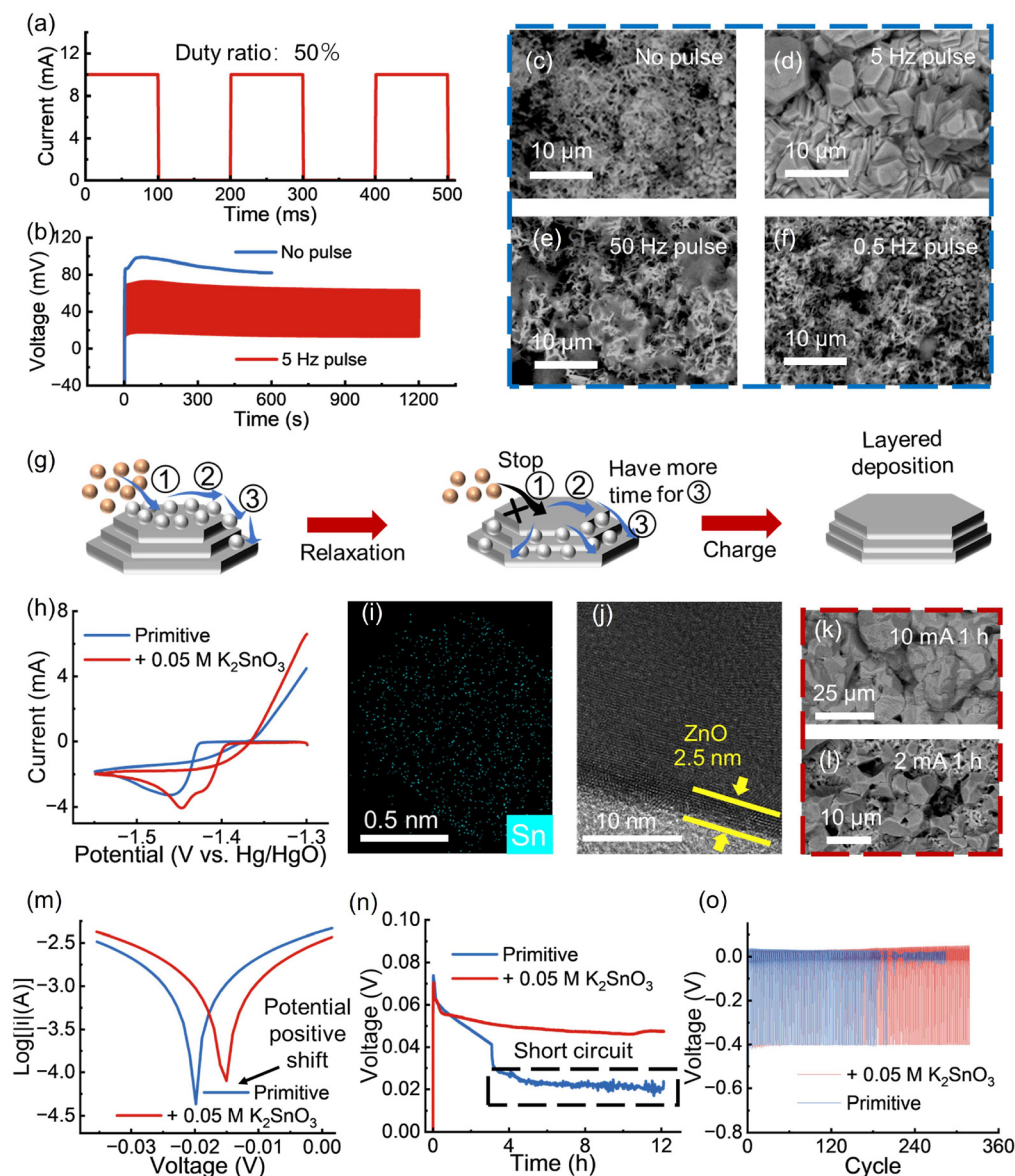


**Fig. 7** Pulse charging and addition of the  $\text{K}_2\text{SnO}_3$  additive. (a) Pulse current profile. (b) Voltage curves with and without pulse current. (c–f) Deposition morphology images under (c) no pulse, (d) 5 Hz, (e) 50 Hz, and (f) 0.5 Hz conditions. (g) Schematic diagram of the effect of pulse on deposition. (h) Comparison of the CV curves with and without the  $\text{K}_2\text{SnO}_3$  additive. (i) Tin element mapping. (j) HR-TEM image of deposition after adding  $\text{K}_2\text{SnO}_3$  at  $10 \text{ mA cm}^{-2}$  for 60 s. (k and l) Morphologies after deposition with  $\text{K}_2\text{SnO}_3$  added at (k)  $10 \text{ mA cm}^{-2}$  and (l)  $2 \text{ mA cm}^{-2}$  for 1 h. (m) Tafel corrosion tests of deposits with and without the  $\text{K}_2\text{SnO}_3$  additive. (n) Short-circuit tests with and without the  $\text{K}_2\text{SnO}_3$  additive. (o) Long-term cycling test with the  $\text{K}_2\text{SnO}_3$  additive.

trollyte group begins to drop rapidly and fluctuates within 4 hours, suggesting a short circuit. In contrast, the voltage in the additive group remains stable even after 12 hours (Fig. 7n). Upon disassembling the two cells, the morphologies of the negative electrodes are shown in Fig. S17a and b. In the additive group, most of the deposits are dense and silvery white, with only a small portion extending from the bottom of the electrode. In the control group, however, the deposits are loose and grayish black, connecting to the positive electrode starting from the middle of the current collector. This finding indicates that the suppression of mossy deposition by  $\text{K}_2\text{SnO}_3$  is beneficial for

battery operation. Finally, long-term cycling tests of Zn–Cu half-cells were conducted. Both the additive group and the pristine group were subjected to charge and discharge cycles at a current density of  $5 \text{ mA cm}^{-2}$ , with 10 minutes each for charging and discharging, and a discharge cutoff voltage of  $-0.4 \text{ V}$ . The voltage curves are shown in Fig. 7o. The pristine group experienced a short circuit as early as the 177th cycle, while the Sn additive group remained normal even after 304 cycles. Additionally, the overpotential of the Sn additive group was initially smaller than that of the pristine group, as shown in Fig. S18. Later, the overpotential of the pristine group gradually





decreased due to the occurrence of micro-short circuits. The coulombic efficiencies of the two groups before the short circuit are shown in Fig. S19. For most of the cycles, the coulombic efficiency of the additive group was higher than that of the pristine group. The average coulombic efficiencies over 176 cycles were 98.35% and 96.68% for the two groups, respectively, indicating that the morphology improved by the Sn additive contributes to performance enhancement.

## Conclusions

In aqueous zinc-based batteries, the mossy Zn deposition morphology is a major factor limiting battery performance and cycling life. This study initially investigated the effects of concentration and polarization degree on nucleation from the traditional nucleation perspective. By decoupling the conditions for nucleation and growth, it is demonstrated that nucleation is not the root cause of mossy morphology. Through morphology observation, XRD analysis, and TEM characterization, it was found that the mossy structure originates from whiskers protruding from the basal facet, which bend repeatedly during growth, accompanied by transformations in the crystal facets. To explain how whiskers form from the basal surface, CV tests and DFT calculations were performed, revealing that the charge transfer step is fast, whereas the interlayer diffusion of Zn adatoms is the rate-determining step. This leads to the accumulation of Zn atoms on the surface and promotes one-dimensional whisker growth. Furthermore, high concentrations lead to the generation of more Zn adatoms, and low polarization results in thicker oxide layers on the deposit, both of which hinder interlayer diffusion and thus favour the formation of mossy deposition. Under neutral electrolyte conditions, a mossy morphology is less frequently observed because of slower reaction kinetics and a sluggish charge transfer process. Finally, based on the proposed mechanism, the rationality of the theory was verified by employing pulsed charging and  $\text{K}_2\text{SnO}_3$  additives. Although these two strategies operate through different mechanisms, both target the key step of interlayer diffusion: pulsed charging addresses kinetic limitations by providing diffusion time, while the  $\text{K}_2\text{SnO}_3$  additive optimizes the diffusion pathway by improving the surface state. These strategies offer practical guidance for suppressing mossy morphology and optimizing the performance of aqueous zinc-based batteries and provide valuable insights for suppressing mossy deposition in other metal battery systems (Fig. S20).

## Materials and methods

### Battery assembly

In this work, Zn–Cu half cells were used to study the effects of electrolyte concentration and current density on the deposition morphology. The positive and negative electrodes were copper and Zn foils, respectively, each with a thickness of 0.05 mm and a purity greater than 99.99%. The electrodes were cut into circular disks with a diameter of 1 cm. The cells were

assembled *via* an acrylic clamp with an interelectrode distance of 5 mm, and a stainless steel mesh served as the current collector. For the concentration-dependent experiments, the electrolyte consisted of 6 M KOH with 0.1–0.4 M ZnO. For the current density tests, the electrolyte was 6 M KOH with 0.4 M ZnO. Cyclic voltammetry (CV) was conducted *via* a three-electrode setup with a glassy carbon working electrode, a Zn counter electrode, and a Hg/HgO reference electrode. The electrolyte composition was the same as that used in the concentration–morphology tests, and the tests were carried out in a 50 mL electrochemical cell. The batteries used for the current density–overpotential test, nucleation and growth morphology test, mossy morphology reversibility test, substrate influence test, EIS test, and pulse and additive tests were the same as those used in the current density–morphology influence experiments. The batteries used for the chronoamperometric test, nucleation morphology tests under different conditions, moss growth process test, and those for TEM imaging were the same as those used in the CV test experiments. In tests involving  $\text{K}_2\text{SnO}_3$ , the electrolyte for the experimental group consisted of 6 M KOH, 0.4 M ZnO, and 0.05 M  $\text{K}_2\text{SnO}_3$ . The CV cell setup was the same as that used in the previously described CV tests, whereas all other measurements followed the configuration used in the current density–morphology experiments.

### Testing

The morphology tests at different concentrations and current densities, measurements of the nucleation overpotential at various current densities, morphology evolution influenced by nucleation and growth, reversibility of mossy deposition, short-circuiting behavior under pulse or  $\text{K}_2\text{SnO}_3$  addition, and coulombic efficiency measurements were conducted using a NEWAR battery tester (CT4008Tn). All other electrochemical measurements were performed using an Admiral Squidstat<sup>TM</sup> Prime workstation. For morphology tests at different concentrations, a current density of  $10 \text{ mA cm}^{-2}$  was applied with a deposition time of 10 minutes. For the morphology tests at different current densities, the applied current densities were 10, 20, 25, and  $30 \text{ mA cm}^{-2}$ , with the same deposition capacity as above. For the CV tests at different concentrations, the voltage scan range was from  $-1.3 \text{ V}$  to  $-1.55 \text{ V}$ , with a scan rate of  $5 \text{ mV s}^{-1}$ . For the nucleation overpotential measurements at different current densities, 1, 5, and  $10 \text{ mA cm}^{-2}$  were used with a charge time of 3000 s. In the chronoamperometric tests at different concentrations, the applied voltage was  $-1.5 \text{ V}$ , and for the tests at different voltages, the applied voltages were  $-1.50$ ,  $-1.55$ ,  $-1.57$ , and  $-1.60 \text{ V}$  with a duration of 12 s. In the nucleation tests at varying concentrations, the applied current density was  $10 \text{ mA cm}^{-2}$  with durations of 1 s and 2 s. In the nucleation tests at different current densities, another set was conducted at  $20 \text{ mA cm}^{-2}$  for 0.5 s and 1 s. For the morphology studies investigating the influence of nucleation and growth, four deposition protocols were used:  $10 \text{ mA cm}^{-2}$  for 10 min;  $25 \text{ mA cm}^{-2}$  for 4 min;  $10 \text{ mA cm}^{-2}$  for 50 s followed by  $25 \text{ mA cm}^{-2}$  for 220 s; and  $25 \text{ mA cm}^{-2}$  for 20 s fol-



lowed by  $10 \text{ mA cm}^{-2}$  for 550 s. In the test assessing whether mossy deposition is reversible,  $10 \text{ mA cm}^{-2}$  was first applied for 10 minutes, followed by  $25 \text{ mA cm}^{-2}$  for 4 minutes. To test the substrate effect on the mossy growth, the reverse sequence was used:  $25 \text{ mA cm}^{-2}$  for 4 minutes followed by  $10 \text{ mA cm}^{-2}$  for 10 minutes. In the time-dependent mossy growth study, a current density of  $20 \text{ mA cm}^{-2}$  was applied for 20, 80, and 400 s. For the CV tests at 0.4 M ZnO at different scan rates, the scan rates were 20, 40, 60, and  $80 \text{ mV s}^{-1}$ , and the voltage ranges were  $-1.3$  to  $-1.5 \text{ V}$ ,  $-1.55 \text{ V}$ ,  $-1.6 \text{ V}$ , and  $-1.6 \text{ V}$ , respectively. For the CV tests at 0.1 M ZnO, the scan rates were the same, with voltage ranges of  $-1.3$  to  $-1.6 \text{ V}$ ,  $-1.65 \text{ V}$ ,  $-1.65 \text{ V}$ , and  $-1.7 \text{ V}$ . For oxygen characterization, the current density was  $20 \text{ mA cm}^{-2}$  for 30 s. For the zinc oxide layer thickness study at different current densities,  $20 \text{ mA cm}^{-2}$  and  $10 \text{ mA cm}^{-2}$  were used for 30 and 60 s, respectively. EIS measurements at different voltages were carried out at 10, 30, and 50 mV, with a bias voltage of 5 mV and a frequency range from 1000 kHz to 100 mHz. For the pulse tests, a current density of  $10 \text{ mA cm}^{-2}$  was applied with a 50% duty cycle and frequencies of 0.5, 5, and 50 Hz for a duration of 20 minutes. In the CV tests with  $\text{K}_2\text{SnO}_3$  addition, the voltage scan ranged from  $-1.3 \text{ V}$  to  $-1.55 \text{ V}$  at a scan rate of  $5 \text{ mV s}^{-1}$ . For elemental Sn and oxide layer thickness characterization, a current density of  $10 \text{ mA cm}^{-2}$  was applied for 60 s. In morphology tests with  $\text{K}_2\text{SnO}_3$  addition, current densities of  $10 \text{ mA cm}^{-2}$  and  $2 \text{ mA cm}^{-2}$  were applied for 1 hour each. For corrosion Tafel measurements of the deposits, deposition was first performed at  $10 \text{ mA cm}^{-2}$  for 10 minutes, followed by a voltage sweep from  $-0.4 \text{ V}$  to  $0.4 \text{ V}$  at a scan rate of  $5 \text{ mV s}^{-1}$ . For short-circuit tests, the current density was  $10 \text{ mA cm}^{-2}$  for 12 hours. For the coulombic efficiency measurements, charging at  $10 \text{ mA cm}^{-2}$  for 10 minutes was followed by a 12-hour rest, after which the samples were discharged at the same current density with a cut-off voltage of  $-0.4 \text{ V}$ .

### Characterization

To observe the microscopic surface morphology of the deposits, the electrode surface was rinsed with deionized water after deposition, followed by drying in a vacuum oven for 1 hour. SEM (Phenom Scientific) was then used for observation, with an accelerating voltage of 15 kV. To determine the crystallographic orientation of the deposits, the electrode surface was similarly rinsed with deionized water after deposition and dried in a vacuum oven for 1 hour, after which XRD (Rigaku SmartLab) analysis was performed with a scan range of  $20$ – $80^\circ$  and a scan rate of  $10^\circ \text{ min}^{-1}$ . To observe and measure the lattice spacing of the deposits, after deposition on a glassy carbon electrode, the surface was rinsed with deionized water, and the deposits were gently brushed off and dispersed in anhydrous ethanol. A drop of the suspension was placed on an ultrathin copper grid and air-dried, followed by observation *via* TEM (JEM-2100F) with an accelerating voltage of 200 kV. The XRD tests were performed at the Physical and Chemical Science Laboratory Center of the USTC. The TEM tests were

performed at the Experimental Center for Engineering and Materials Science of the USTC.

### Theoretical calculation

All the DFT calculations were conducted with the Vienna *Ab initio* Simulation Package (VASP).<sup>48,49</sup> The exchange–correlation effects were described by the Perdew–Burke–Ernzerhof (PBE) functional within the generalized gradient approximation (GGA) method.<sup>50,51</sup> The core–valence interactions were accounted for using the projected augmented wave (PAW) method.<sup>52</sup> The energy cut-off for facet wave expansion was set to 480 eV, and  $3 \times 3 \times 1$  Monkhorst–Pack grid *k*-points were selected to sample the Brillouin zone integration. The vacuum space was adopted 15 Å above the surfaces to avoid periodic interactions. The structural optimization was completed for energy and force convergence set at  $1.0 \times 10^{-4} \text{ eV}$  and  $0.02 \text{ eV Å}^{-1}$ , respectively. The energy profiles of the Zn ion migration of the material were calculated *via* the method of a climbing image nudged elastic band (CI-NEB).

### Author contributions

Jianwen Yu: conceptualization, methodology, investigation, and writing – original draft preparation; Zhongxi Zhao: investigation and methodology; Zhuojun Zhang: investigation; Jiangfeng Huang: visualization; Peng Tan: conceptualization, writing – review & editing, supervision, project administration, and funding acquisition.

### Conflicts of interest

There are no conflicts to declare.

### Data availability

All relevant data are included within the article and its supplementary information (SI). Supplementary information is available. See DOI: <https://doi.org/10.1039/d5eb00178a>.

### Acknowledgements

We thank the funding support from the Students' Innovation and Entrepreneurship Foundation of USTC (SC5290005336) and the National Innovative Talents Program (GG2090007001). This work was partially carried out at the Instruments Center for Physical Science, University of Science and Technology of China. The authors also thank Huijuan Wang for her support in the characterization.



## References

- 1 D. Ma, F. Li, K. Ouyang, Q. Chen, J. Zhao, M. Chen, M. Yang, Y. Wang, J. Chen, H. Mi, C. He and P. Zhang, *Nat. Commun.*, 2025, **16**, 4817.
- 2 W. Ling, F. Mo, X. Wu, X. Zeng, J. Xiong and Y. Huang, *Nat. Commun.*, 2025, **16**, 4868.
- 3 M. Zhao, Y. Lv, Y. Xu, H. Yang, Z. Bo and J. Lu, *Nat. Commun.*, 2025, **16**, 2843.
- 4 J. S. Cha, S. Park, N.-U. Seo, Y.-C. Kang, C.-W. Lee and J. H. Yang, *Nat. Commun.*, 2025, **16**, 844.
- 5 D. Dong, T. Wang, Y. Sun, J. Fan and Y.-C. Lu, *Nat. Sustainability*, 2023, **6**, 1474–1484.
- 6 S. Nanda, A. Gupta and A. Manthiram, *Adv. Energy Mater.*, 2021, **11**, 2000804.
- 7 A. J. Louli, A. Eldesoky, R. Weber, M. Genovese, M. Coon, J. deGooyer, Z. Deng, R. T. White, J. Lee, T. Rodgers, R. Petibon, S. Hy, S. J. H. Cheng and J. R. Dahn, *Nat. Energy*, 2020, **5**, 693–702.
- 8 P. Liang, H. Sun, C. Huang, G. Zhu, H. Tai, J. Li, F. Wang, Y. Wang, C. Huang, S. Jiang, M. Lin, Y. Li, B. Hwang, C. Wang and H. Dai, *Adv. Mater.*, 2022, **34**, 2207361.
- 9 Q. Yang, Q. Li, Z. Liu, D. Wang, Y. Guo, X. Li, Y. Tang, H. Li, B. Dong and C. Zhi, *Adv. Mater.*, 2020, **32**, 2001854.
- 10 L. Cao, D. Li, T. Pollard, T. Deng, B. Zhang, C. Yang, L. Chen, J. Vatamanu, E. Hu, M. J. Hourwitz, L. Ma, M. Ding, Q. Li, S. Hou, K. Gaskell, J. T. Fourkas, X.-Q. Yang, K. Xu, O. Borodin and C. Wang, *Nat. Nanotechnol.*, 2021, **16**, 902–910.
- 11 H. Tian, G. Feng, Q. Wang, Z. Li, W. Zhang, M. Lucero, Z. Feng, Z.-L. Wang, Y. Zhang, C. Zhen, M. Gu, X. Shan and Y. Yang, *Nat. Commun.*, 2022, **13**, 7922.
- 12 A. Jana, S. I. Woo, K. S. N. Vikrant and R. E. García, *Energy Environ. Sci.*, 2019, **12**, 3595–3607.
- 13 J. Xiao, *Science*, 2019, **366**, 426–427.
- 14 D. Wang, W. Zhang, W. Zheng, X. Cui, T. Rojo and Q. Zhang, *Adv. Sci.*, 2017, **4**, 1600168.
- 15 Q. Yang, G. Liang, Y. Guo, Z. Liu, B. Yan, D. Wang, Z. Huang, X. Li, J. Fan and C. Zhi, *Adv. Mater.*, 2019, **31**, 1903778.
- 16 J. Y. Kim, G. Liu, G. Y. Shim, H. Kim and J. K. Lee, *Adv. Funct. Mater.*, 2020, **30**, 2004210.
- 17 Z. Yi, *Microstructure Studies of Zinc Electrodeposits in Zinc Metal Batteries*, Ph.D., The Hong Kong University of Science and Technology, 2024.
- 18 J. X. K. Zheng, J. Yin, T. Tang and L. A. Archer, *ACS Energy Lett.*, 2023, **8**, 2113–2121.
- 19 T. Otani, Y. Fukunaka and T. Homma, *Electrochim. Acta*, 2017, **242**, 364–372.
- 20 R. Y. Wang, D. W. Kirk and G. X. Zhang, *ECS Trans.*, 2007, **2**, 19–27.
- 21 T. Otani, M. Nagata, Y. Fukunaka and T. Homma, *Electrochim. Acta*, 2016, **206**, 366–373.
- 22 Q. Zou, Z. Liang, W. Wang, D. Dong and Y.-C. Lu, *Energy Environ. Sci.*, 2023, **16**, 6026–6034.
- 23 Y. Li, P. Wu, W. Zhong, C. Xie, Y. Xie, Q. Zhang, D. Sun, Y. Tang and H. Wang, *Energy Environ. Sci.*, 2021, **14**, 5563–5571.
- 24 Z. Wang, X. Zhu, X. Tao, P. Feng, J. Wang and J. Chen, *Adv. Funct. Mater.*, 2024, **34**, 2316223.
- 25 S. Wang, Z. Wang, Y. Yin, T. Li, N. Chang, F. Fan, H. Zhang and X. Li, *Energy Environ. Sci.*, 2021, **14**, 4077–4084.
- 26 D. Desai, *Nucleation and growth in alkaline zinc electrodeposition*, Ph.D., The City College of New York, 2015.
- 27 C. Cachet, B. Saïdani and R. Wiart, *Electrochim. Acta*, 1988, **33**, 405–416.
- 28 A. H.-L. Goff, S. Joiret, B. Saïdani and R. Wiart, *J. Electroanal. Chem.*, 1989, **263**, 127–135.
- 29 C. Cachet, B. Saïdani and R. Wiart, *Electrochim. Acta*, 1989, **34**, 1249–1250.
- 30 C. Xie, S. Liu, Z. Yang, H. Ji, S. Zhou, H. Wu, C. Hu, Y. Tang, X. Ji, Q. Zhang and H. Wang, *Angew. Chem., Int. Ed.*, 2023, **62**, e202218612.
- 31 X. Wang, W. Zeng, L. Hong, W. Xu, H. Yang, F. Wang, H. Duan, M. Tang and H. Jiang, *Nat. Energy*, 2018, **3**, 227–235.
- 32 W. Shi, Z. Song, W. Zhang, S. Lian, F. Huang, Q. An and Q. Li, *Energy Environ. Sci.*, 2024, **17**, 7372–7381.
- 33 Z. Wang, J. Diao, G. Henkelman and C. B. Mullins, *Adv. Funct. Mater.*, 2024, **34**, 2314002.
- 34 Y. Zeng, P. X. Sun, Z. Pei, Q. Jin, X. Zhang, L. Yu and X. W. (David) Lou, *Adv. Mater.*, 2022, **34**, 2200342.
- 35 C. Wu, C. Sun, K. Ren, F. Yang, Y. Du, X. Gu, Q. Wang and C. Lai, *Chem. Eng. J.*, 2023, **452**, 139465.
- 36 B. Li, S. Liu, Y. Geng, C. Mao, L. Dai, L. Wang, S. C. Jun, B. Lu, Z. He and J. Zhou, *Adv. Funct. Mater.*, 2024, **34**, 2214033.
- 37 X. Shi, G. Xu, S. Liang, C. Li, S. Guo, X. Xie, X. Ma and J. Zhou, *ACS Sustainable Chem. Eng.*, 2019, **7**, 17737–17746.
- 38 J. Yu, L. Wang, L. Su, X. Ai and H. Yang, *J. Electrochem. Soc.*, 2003, **150**, C19.
- 39 J. C. Ballesteros, P. Díaz-Arista, Y. Meas, R. Ortega and G. Trejo, *Electrochim. Acta*, 2007, **52**, 3686–3696.
- 40 M.-J. Deng, P.-C. Lin, J.-K. Chang, J.-M. Chen and K.-T. Lu, *Electrochim. Acta*, 2011, **56**, 6071–6077.
- 41 S. E. R. Tay, A. E. Goode, J. Nelson Weker, A. A. Cruickshank, S. Heutz, A. E. Porter, M. P. Ryan and M. F. Toney, *Nanoscale*, 2016, **8**, 1849–1853.
- 42 L. Miao, W. Jia and L. Jiao, *Chem. Sci.*, 2024, **15**, 18227–18238.
- 43 H. Zhang, M. Ulusel and F. Shi, *ACS Appl. Mater. Interfaces*, 2024, **16**, 66971–66980.
- 44 T. Shen, T. Wei, S. Zhang, H. Liu, C. Li, Z. Li, M. Yang, C. Liu and Y. Pei, *Small Struct.*, 2025, **6**, 2400325.
- 45 Y. Wang, Z. Deng, B. Luo, G. Duan, S. Zheng, L. Sun, Z. Ye, J. Lu, J. Huang and Y. Lu, *Adv. Funct. Mater.*, 2022, **32**, 2209028.
- 46 T. Mitsuhashi, Y. Ito, Y. Takeuchi, S. Harada and T. Ujihara, *Thin Solid Films*, 2015, **590**, 207–213.
- 47 A. Komiya, T. Wang, M. Kunitomo, T. Asano, Y. Nishikitani and T. Homma, *J. Power Sources*, 2025, **626**, 235714.
- 48 G. Kresse and J. Hafner, *Phys. Rev. B: Condens. Matter Mater. Phys.*, 1993, **47**, 558–561.





- 49 G. Kresse and J. Hafner, *Phys. Rev. B: Condens. Matter Mater. Phys.*, 1994, **49**, 14251–14269.
- 50 J. P. Perdew, K. Burke and M. Ernzerhof, *Phys. Rev. Lett.*, 1996, **77**, 3865–3868.
- 51 G. Kresse and D. Joubert, *Phys. Rev. B: Condens. Matter Mater. Phys.*, 1999, **59**, 1758–1775.
- 52 P. E. Blöchl, *Phys. Rev. B: Condens. Matter Mater. Phys.*, 1994, **50**, 17953–17979.

